NPL
National Physical Laboratory

NPL REPORT MAT 125

UNCERTAINTIES IN SCANNING ELECTRON MICROSCOPY – DIMENSIONAL MEASUREMENT CALIBRATION AND ANGULAR MEASUREMENT WITH EBSD

V.TONG AND K.P.MINGARD

DECEMBER 2023

Uncertainties In Scanning Electron Microscopy – Dimensional Measurement Calibration and Angular Measurement With EBSD

V.Tong and K.P.Mingard
Materials and Mechanical Metrology

ABSTRACT

The operation of a range of scanning electron microscopes in one laboratory enables a direct assessment of the variation between measurements made on each of them and thus evaluate the uncertainties involved. This report considers both the typical variability of dimensional measurements from four microscopes operating over a wide range of conditions and, separately, the uncertainty in angular measurement of orientation by electron backscatter diffraction.

The use of linear calibration artefacts for dimensional measurements is discussed and the application of the measurement of dimensional errors is illustrated by verifying the accuracy of gold nanoparticle size distributions and the determination of the uncertainty in these distributions.

EBSD angular uncertainties were assessed by mapping the same area of a single specimen transferred between three microscopes with different EBSD systems on each.

ISSN 1754-2979

https://doi.org/10.47120/npl.MAT125

National Physical Laboratory
Hampton Road, Teddington, Middlesex, TW11 0LW

This work was funded by the UK Government's Department for Science, Innovation & Technology through the UK's National Measurement System programmes.

Approved on behalf of NPLML by
Stefanos Giannis, Science Area Leader.

CONTENTS

1. INTRODUCTION

To ensure the accuracy of dimensional measurements from scanning electron microscope (SEM) images, international standards (ISO16700:2004 [1] and ASTM E766-14 [2]) refer in their titles to calibration of image magnification. These titles obscure the fact that for images acquired digitally by modern microscopes, use of the term magnification can be misleading for a number of reasons:

i) Most obviously, magnification is dependent on the size with which an image is reproduced, and digital images can be easily enlarged or shrunk to suit a display or document.
ii) In practice, it is the image pixel size that is critical in allowing measurements to be made with digital software. In fact, two images with identical magnification can be acquired comprised of an order of magnitude different number of pixels, with resultant effects on the resolution and size of feature that can be measured.
iii) A corollary of i) is that specification of a required image magnification can lead to confusion and acquisition of either an unrepresentatively small area, or of insufficient detail. The critical parameters to specify are the image (horizontal) field width and pixel size.
iv) In practice, the accuracy of dimensional measurements made from a digital image are more likely to be affected by varying image contrast mechanisms or sample orientation and user interpretation than by the calibration of the microscope.

ISO 16700 in particular is in need of significant revision to accommodate the operation of modern digital SEMs.

This report therefore aims to highlight the typical variability in the accuracy of dimensional measurements made to verify SEM calibrations that may be expected from operation of a range of different microscopes operating over a wide range of conditions. It shows the application of the measurement of dimensional errors in verifying the accuracy of gold nanoparticle size distributions and the determination of the uncertainty in these distributions.

Calibration of dimensional measurements is also essential when an SEM is used to produce maps by electron backscatter diffraction (EBSD). Thus this report extends the methods in the standards used on samples oriented perpendicular to the electron beam to samples tilted to the high angles required by EBSD. The errors resulting at these tilt angles are shown to be much larger and reasons for this are discussed.

EBSD mapping also measures the orientation of the crystalline structures that comprise the sample under investigation and these orientations are displayed with various colour scales to show the crystal orientation relative to microscope (and sample) axes. Using three different microscope/EBSD systems to map the same area of a polycrystalline sample, the variability of the resulting measured orientations has been quantified to give an estimate of the typical uncertainty in absolute orientation measured by EBSD. The results also illustrate how subtle variations in the colour scales used to display these orientations can lead to very different visual displays of orientation in some circumstances.

2. DIMENSIONAL MEASUREMENTS CALIBRATION METHODOLOGY

The methodology for image magnification calibration that is discussed in the international standards (ISO16700:2004 [1] and ASTM E766-14 [2]) requires a calibration artefact to be measured under as near to identical conditions as for the sample to be measured, producing a calibration to qualify the images collected at that time, and not suitable for measurements performed at different times or different conditions. This gives the maximum confidence in the calibration but is somewhat restrictive and cumbersome; for example, when multiple accelerating voltages are used to optimise the contrast for different features. Evaluating the variation in errors in measurement of a certified reference material with operating parameters can help, perhaps at the expense of increased uncertainty. These errors can be seen as correction factors that can be applied to any subsequent measurements made under similar conditions. This report includes measurement of these errors or correction factors and shows variation over time and with operator. In particular it includes plots of data to show how the errors vary with operating parameters and especially when samples are tilted .

Historic data included in this report has been acquired on two particular SEMs, a Zeiss Supra 40 and a Zeiss Auriga 60. This has been expanded to include a Zeiss Evo and a ThermoFisher ApreoS2. Details of the different specifications for these microscopes are included in Appendix A. All measurements were made on a certified reference repeating line structure sample (Cr deposited on Si). The sample was a Pelcotec 687-01 CDMS-0.1C, serial No CD-YC01-1519 individually certified directly against a NIST standard. Feature sizes measured ranged from 0.500 mm down to 100 nm.

3. VARIATION BETWEEN MICROSCOPES

3.1. STANDARD FLAT SPECIMEN

Table 1 shows the average percentage error of SEM image dimensions for the Pelcotec sample when mounted flat, over a range of accelerating voltages and magnifications. (Data is grouped by the ‘linewidth’ metric). The data shown is averaged over 3 operators and both X and Y dimensions. For a given accelerating voltage, the working distance and beam current used were as similar as possible to each other and approximated to typical conditions that might be used for that voltage.

Table 1. Average percentage error for different operating conditions on four microscopes

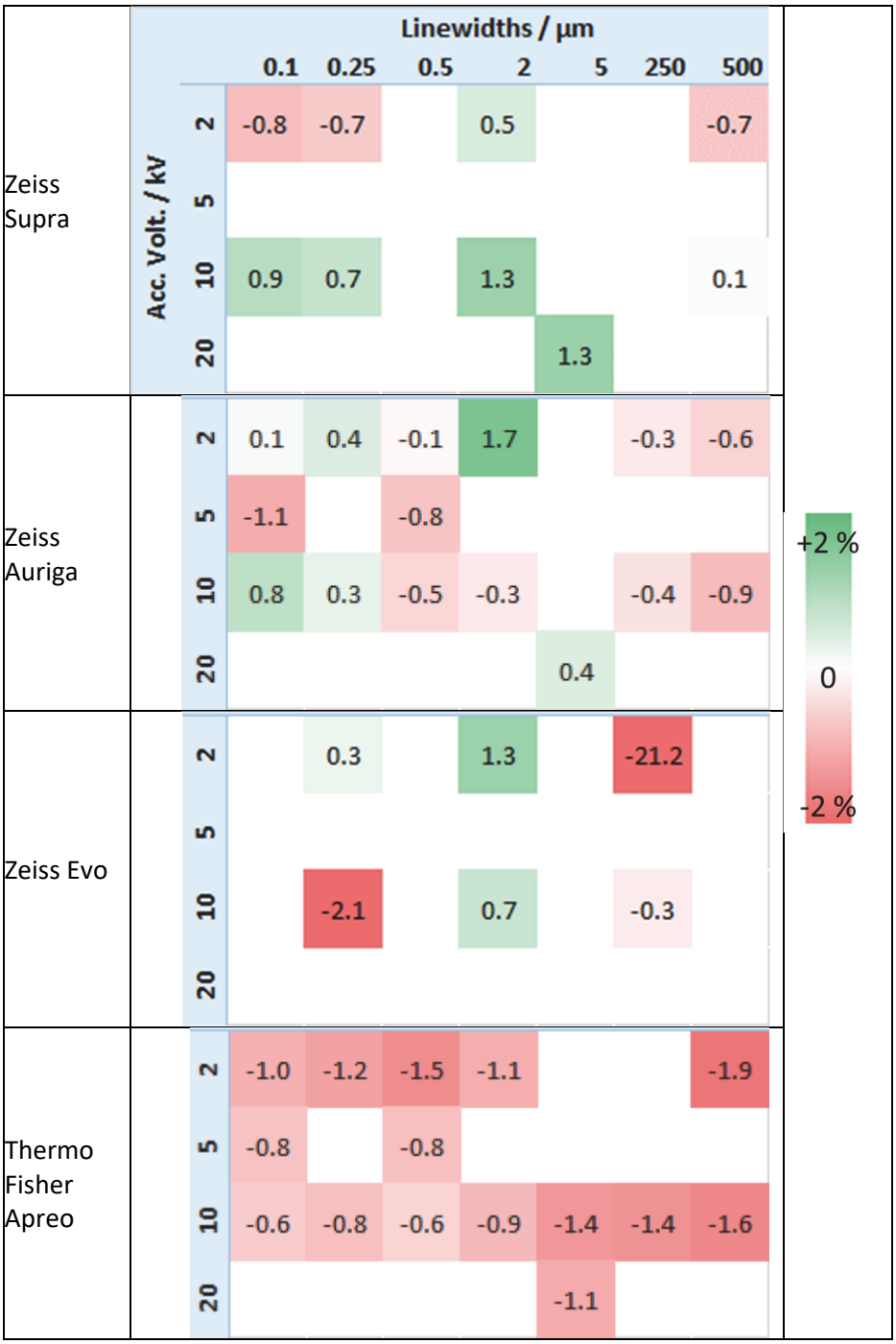

It is clear that, with two exceptions, errors are < 2%, and most < 1%. The Evo is the only W-filament instrument with a less complex column, giving lower resolution than the other field emission source microscopes; it clearly struggled at the low accelerating voltage and low magnification.

There appears to be no systematic pattern to the errors for the two Zeiss microscopes, with positive and negative errors at both accelerating voltages and variation with magnification. The Thermofisher microscope on the other hand showed a consistent negative offset but with less scatter about the mean error.

However, when a single operator covered a wider range of working distances and accelerating voltages on the Zeiss Auriga SEM it is possible to see some slight systematic variation (Table 2). In the preceding Table 1 the variation from combining measurement of both axes and using multiple images from different operators will probably have reduced the average errors and obscured the trend below.

Table 2. Percentage error (one operator) at different working distances (Zeiss Auriga microscope, x-axis measurements only)

Mag Range		1	1	2	2	2	2
Pixel Size (nm)		1960	147	29.39	5.879	2.939	0.5879
Magnification		150	2000	10000	50000	100000	500000
kV	WD						
1	5		-1.53	-1.77	-1.36	-0.76	
5	5	-1.47	-1.09	-0.76	-0.76	-1.24	0.52
5	10	-1.27	-0.35	-0.52	-0.64	-1.00	
5	20	-1.00	-0.21	-0.28	-0.18	0.16	
20	5	-0.60	0.50	0.64	0.42	0.16	0.22
20	10	-1.13	-0.35	0.04	0.31	0.04	
20	20	-1.27	-0.65	-0.04	0.06	0.04	

3.2. EFFECT OF SPECIMEN TILT.

To look at the effect of tilting on measurements, electron beam conditions typical of those used for electron backscatter diffraction (EBSD) were used: 10 - 12 mm working distance, 20 kV (and 10 kV in one case) accelerating voltage and high probe currents. For such an application with a flat surface, SEM software can apply a tilt correction to adjust the gain/scan pitch in the vertical Y direction using an angle of tilt entered by the user or read from the stage tilt. In the latter case and almost always the former, the assumption is made that the imaged surface is parallel to the stage surface. Tilt angles between 0 and 70° were used.

Since the stage tilt axis is along X for all the SEMs used here the tilt-shortened direction in the SEM image is along Y (perpendicular to the tilt axis). All measured lengths were made along Y using the 5 µm lines of the Pelcotec standard. Measurements were also made from images acquired with no tilt correction, in which case the length measured was compared with that expected after applying a trignometric correction for the stage tilt.

In this case, averaging the errors between operators has not been used to compare results for reasons that are obvious when the individual errors are considered in the plots for the three microscopes used in Figure 1 a-c). In all three cases, the errors increase with tilt angle, in the worst cases at an increasing rate, and in the extreme ranging from ≈0% at 0° to -10% at 70°. However, it can be seen that the direction of increase of the errors (i.e. +ve or -ve) changed between operators for two of the microscopes (Figures 1 a and b) or, for the Apreo microscope (Figure 1 a), between sessions with the same operator. In other words, using the Apreo example, operator 1 saw a steady increase in error from (approximately) -1 to +1% when acquiring images at 20 kV while under the

same conditions, but on a separate occasion operator 2 saw a decrease from -1 to -4.5%. However, still on the same microscope, but at 10 kV on a separate occasion, operator 2 also measured a similar +ve trend as operator 1 had done at 20 kV.

It is clear from Figures 1 a and b that the error on the non-tilt corrected image was very close (in magnitude (and identical in sign)) to that measured on the tilt corrected image. This implies that the tilt correction gain applied by the microscope to the scan in the Y direction is correct and has negligible influence on the error. Instead the increasing error must arise because the sample is not tilted at the expected angle. It was assumed that as the Pelcotec standard is a flat silicon wafer on a flat aluminium pin stub it would lie flat on the SEM stage: however, an error of only 1° could produce an error of 5% in the distance measured on a non-tilt corrected image at 70° tilt. A small variation in the glue fixing the standard to the stub could account for small tilt errors, but the apparently random variation in magnitude and direction suggests the possibility that differences in clamping of the stub pin to the SEM stage could have produced small tilts of differing amounts.

The other factor that could particularly affect measurement errors on the tilted sample is image drift in the Y-direction. Observations of mapping of EBSD samples on the Zeiss Supra (Figure 1c) used here have revealed a particular tendency on this microscope for drift in the negative Y direction. However, this would lead to over-estimates of measurement and affect the tilt corrected images more than the non-tilt corrected, contrary to the observations. Unless drift was random in magnitude and direction, it cannot explain the increase in scatter seen for this microscope.

A further factor not quantified here is the effect of dynamic focus; while this can improve the image focus at top and bottom of the image, it also produces some scan rotation and distortion of the image which could influence measurements, particularly if the imaged feature is not centred identically in each image. Figure 2 shows the qualitative effect of this scan rotation distortion: the parallel horizontal line features on the sample appear parallel in the image with dynamic focus turned off (Figure 2a), but not with dynamic focus turned on (Figure 2b). A sample feature would appear longer if imaged on the right than the left side of this image.

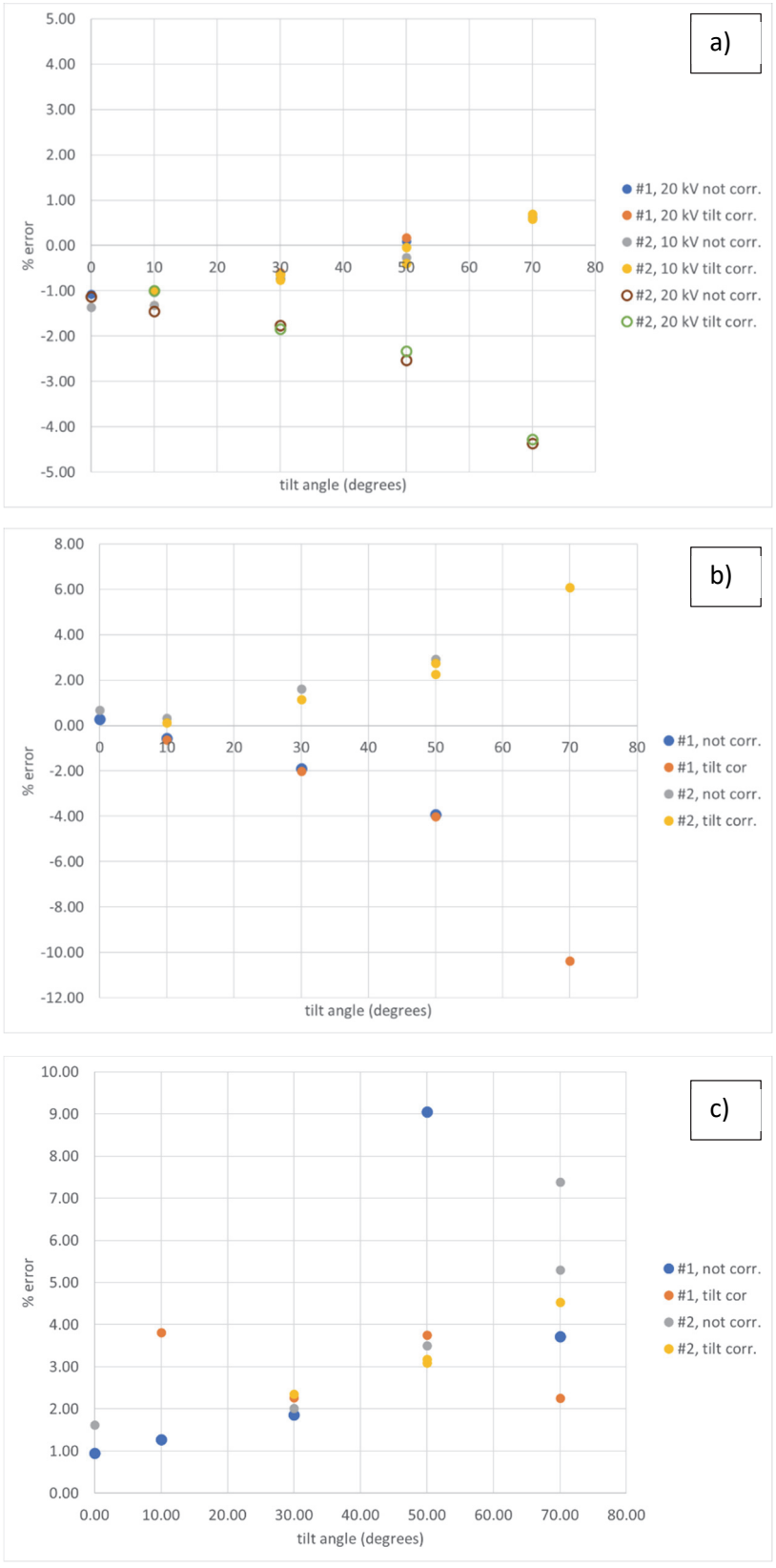

Figure 1. Percentage error in dimensional measurement of 5 µm line spacing reference at different tilt angles for a) Apreo, b) Auriga and c) Supra microscopes. Note different vertical scales.

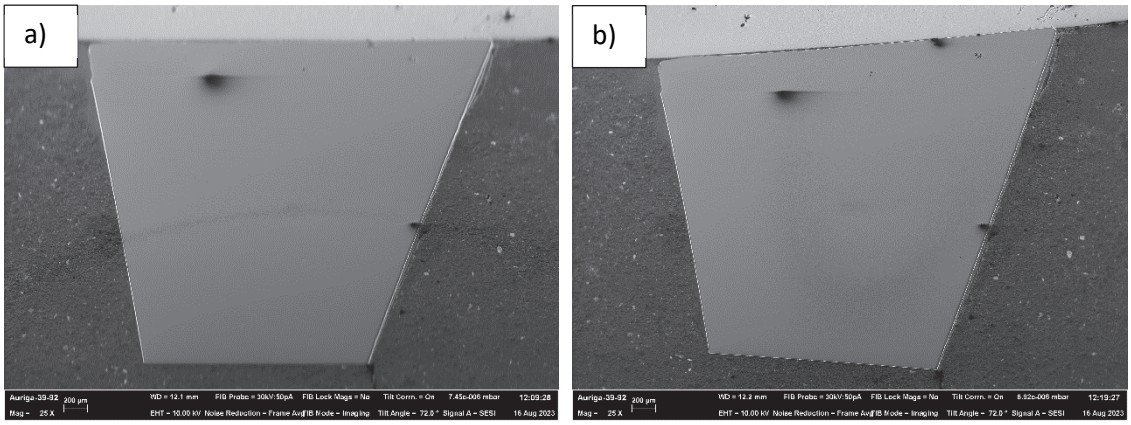

Figure 2. The same field of view on a 70° tilted sample with a) dynamic focus off, and b) dynamic focus on. The image height is 3.456 mm, which means that the working distance increases by 3.25 mm from the bottom to top of the image. Dynamic focus keeps the entire sample surface in focus but introduces scan distortions. (Zeiss Auriga, 10 kV, 120 µm aperture, high current mode on.)

4. VARIATION WITH OPERATOR

4.1. IMAGE ACQUISITION

The data in the first section reported values for errors averaged over three operators and makes the assumption of an isotropic change in pixel size by averaging over X and Y directions. In practice the X and Y scans will have independent gain settings, and, as has been noted on the tilted samples, drift can affect one axis more than the other. The following Figures 2a and b show individual results in both X and Y directions by 5 operators measuring their own acquired images, for both the Zeiss Supra and Auriga microscopes, and covering a similar range of pixel sizes to the previous data. Most errors are within a range very similar in magnitude and sign to that of the data in Table 1, suggesting a high degree of stability for the two microscopes as the two sets of data (Table 1, Figure 3) were acquired nearly 2 years apart, with no alteration to the microscope calibrations at services between these times.

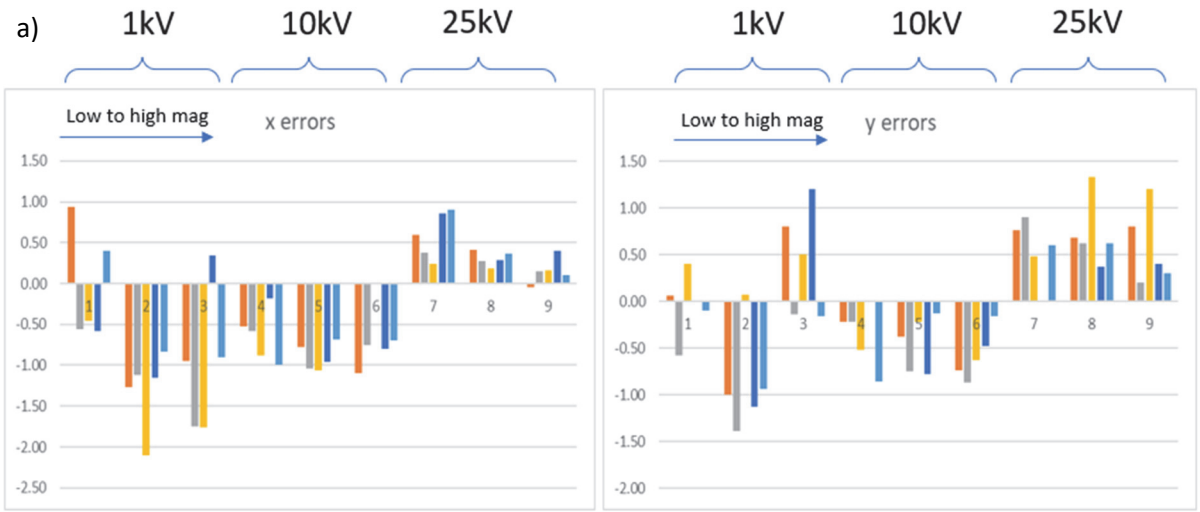

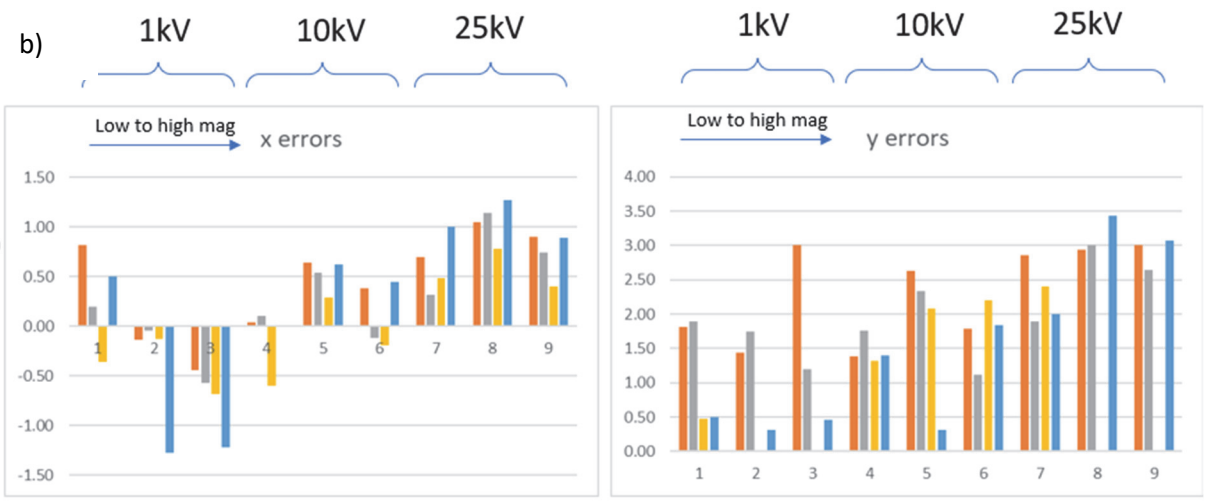

Figure 3. individual measurements of percentage errors on measurement of Pelcotec CRM by five different operators on a) Auriga and b) Supra SEMs. The three sets of data at each accelerating voltage refer to measurements on line width samples of 500 µm, 2 µm and 250 nm respectively.

The most obvious variation seen is that there is a much larger error for the Supra Y direction than for any other set of measurements; that this Y-error increases with accelerating voltage may indicate a tendency to drift caused by increased sample charging. However, more generally for the other conditions, there is no clear trend in the magnitude of the errors with accelerating voltage, nor with increasing magnification at a given voltage. The sign of the error tends to be consistent for a given accelerating voltage and switching from a negative to a positive error at higher voltages.

4.2. IMAGE MEASUREMENT

A range of options exists for measurement of dimensions from an image. The simplest method can be to use software provided as part of the microscope operating software which enables the drawing of a cursor between two points with the distance between them displayed on the image. A common alternative is to use software such as ImageJ ((http://imagej.org), entering the image pixel size read from the image metadata to set the scale, and then drawing an appropriate shape to measure the distance between features. Both methods have been used in the following example where images have been measured twice, firstly by the operator acquiring the image using the SEM software and secondly by another person examining the saved image in imageJ. The differences between the % error measured by the operator and the repeat measurements of the second person are shown in Figure 4. Thus two sets of original results (i.e. from the two operators) are compared with repeat measurements by just one person; the repeat measurement method should therefore have been consistent across all the images. In most cases the second person measured an error that differed from the original operator measurement by +/- 0.5% ; in comparison with operator 2 the agreement was good, but with a constant offset such that operator 2 consistently measured about -0.25% smaller than the second person. With operator 2 the differences were more random.

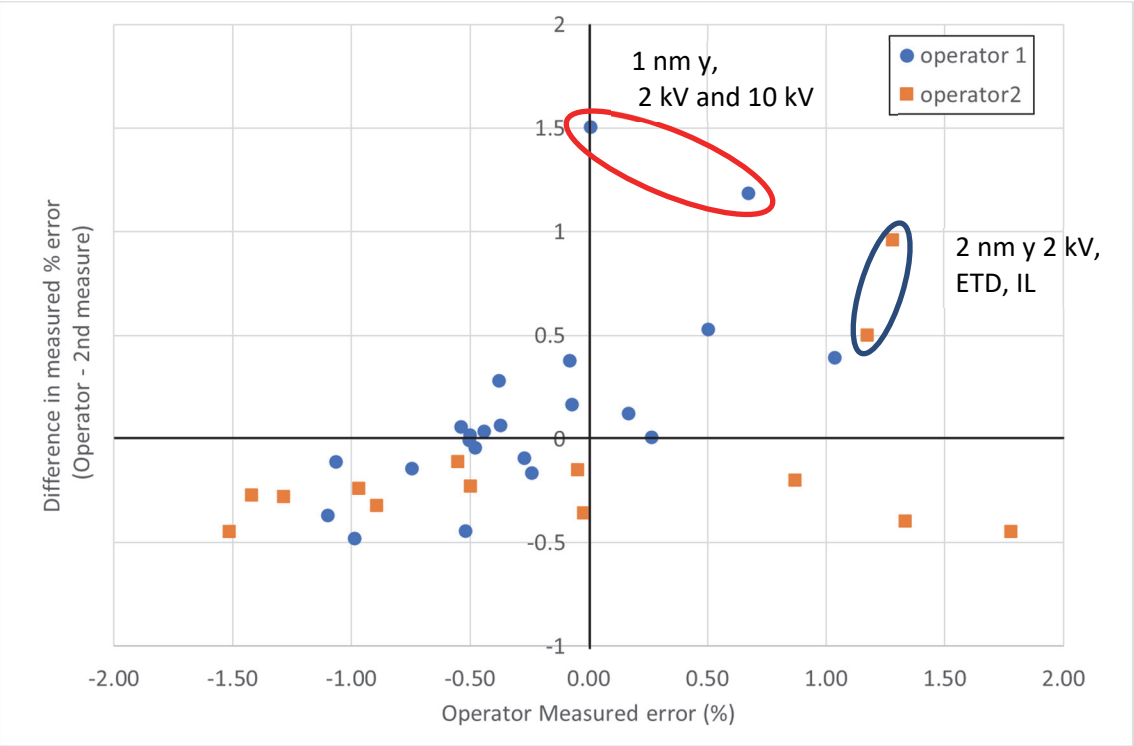

Figure 4. Plot showing the difference in % error between repeat measurements by a second person using ImageJ and those of two operators using SEM software.

Two sets of measurements stand out as being different from the other, and possibly significantly these are both for measurements in the Y direction on high magnification images. These would have covered only a relatively few (5 or 6) lines of the calibration standard compared with 8-12 at lower magnifications or in the X direction. Taking one of these images of the 2 nm pixel size image of 250 nm line spacing as an example, Figure 5a shows some possible individual measurements with the SEM software while Figure 5b shows the approach used with imageJ. Both illustrate a number of issues with manual measurement. Figure 5a shows on the left a single measurement between the centres (as recommended for this standard) of lines crossing the maximum distance on the image; in practice an average is taken of multiple measurements like this from across the width of the sample but care must be taken to remove each preceding measurement to avoid biasing positioning of the subsequent ones. If there is very good alignment with the scan axes an alternative is to use a wide cursor to align with the centres or, as shown here the line edges, to average out variation across the image width. Measurements on this image are clearly subject to user interpretation of the line centre or edge, and when there are few lines measured this also adds to the potential size of the error.

These issues still apply to use of imageJ, but Figure 5b shows some additional points that can minimise the errors. Firstly, rotating the image so the lines are vertical can reduce errors from needing to look at different angles towards the top and bottom of an image on a large screen. Secondly use can be made of averaging of the brightness profile within a box width and then using a common peak height/feature on each line profile to determine the edge or centre positions.

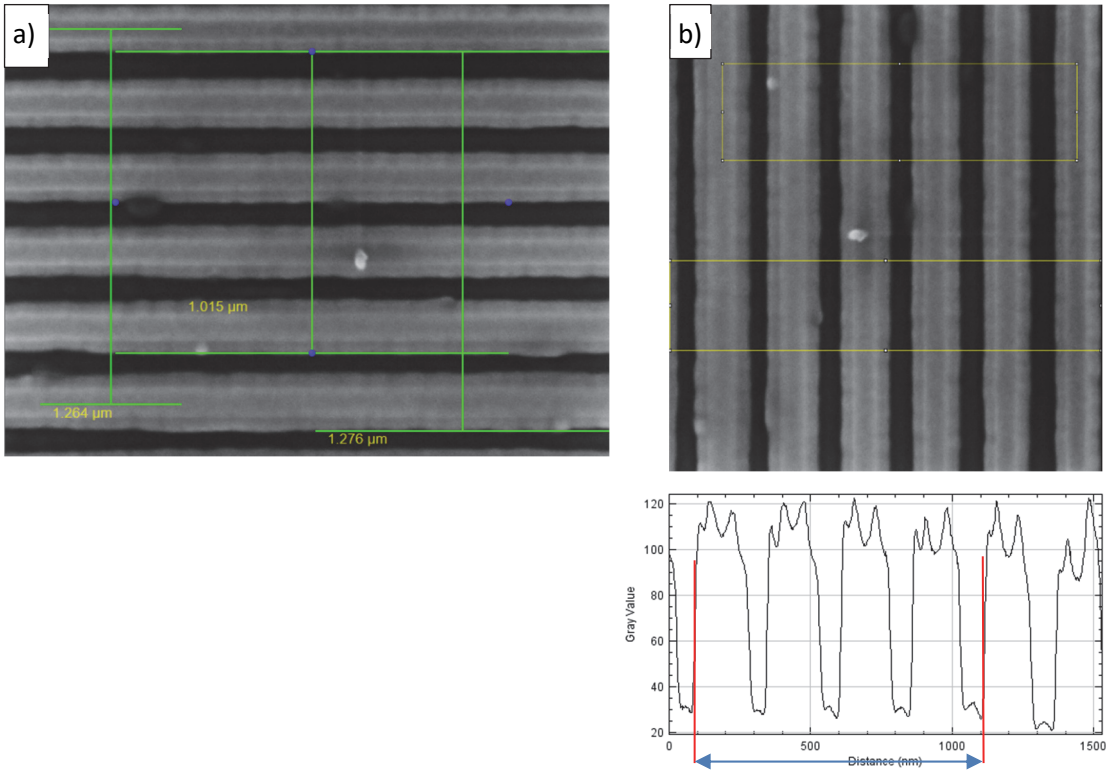

Figure 5. a) Image measurement using SmartTiff v3.00. b) the same image rotated by 90° in ImageJ and measuring either the top box width or using the brightness profile from within the lower box and then identifying the distance between peak half-heights.

It has also been noted that the cursor width of the SEM software and different versions of this software can lead to differences of 3-4 pixels in measurements. In the above case this could produce an offset of up to 6 nm or 0.5% which is similar to differences in errors seen in Figure 4.

5. APPLICATION TO NANOPARTICLE MEASUREMENT

5.1. SEM IMAGING OF NANOPARTICLES

Dimensional measurements of SEM image features depend not only on the pixel size calibration, but also on the contrast of the measured features. The following case study demonstrates size measurement of two gold nanoparticle samples, 'Au30' and 'Au60'. Their respective average diameters were 32.7 ± 2.0 nm (k=2, measured by particle tracking analysis) and approximately 60 nm. Nanoparticles were deposited onto 200-mesh, carbon-coated copper TEM grids for SEM imaging. The TEM grid surface was functionalised with Alcian Blue dye before particle deposition to minimise particle agglomeration on the TEM grid surface.

The projected areas of the gold nanoparticles were measured using bright-field transmission scanning electron microscopy (BF-TSEM) imaging, using a ThermoFisher Apreo 2 S LowVac scanning electron microscope operating at 10 kV accelerating voltage, 50 pA probe current, and 10 mm working distance. The SEM was controlled using ThermoFisher XT-UI v23.3 software and images were acquired using ThermoFisher Maps v3 software. Images were acquired at 4096 × 3536 pixels with nominal pixel sizes of 1 nm for Au30 and 2 nm for Au60, and saved as 16-bit TIFF files (2^{16} = 65536 grey levels).

For the Au60 sample, 403 isolated particles were analysed from 308 images acquired across 5 grid squares on two separate TEM grids. For the Au30 sample, 4950 isolated particles were analysed from 96 images acquired within a single TEM grid square. Example images are shown in Figures 6 and 8.

Image analysis for particle size was performed using in-house written MATLAB software (MATLAB R2023a, Mathworks Inc.) using a similar method to the one reported in Meli et al. 2012 [4]. This imaging mode produced dark particles on a bright background, and edge brightening artefacts were not observed. The particle contour was drawn according to a fractional threshold between the grey level at the centre of each particle and the grey level in the surrounding background pixels as shown in the examples in Figures 6d and 8d.

The threshold value at the physical particle boundary depends on the particle size and can in theory be determined for each individual particle using a Monte-Carlo simulation [4]. Since this Monte-Carlo simulation was not available, and the particle size distributions are narrow (standard deviations of 2.84 nm and 6.84 nm for Au30 and Au60 respectively), the fractional threshold was estimated at 0.50, and the effect of changing the fractional threshold between 0.45 and 0.55 was included in the uncertainty model as a rectangular type B uncertainty.

5.2. PIXEL SIZE CALIBRATION

The 100 nm and 500 nm pitch lines of the Pelcotec 687-01 CDMS-0.1C sample described previously were used to calibrate the SEM image pixel size immediately after imaging the nanoparticles using similar imaging conditions and the Everhart-Thornley and in-lens secondary electron detectors. (The BF-TSEM detector could not be used because the reference sample is not electron transparent.)

5.3. UNCERTAINTY MODEL

Uncertainty sources, shown in Table 3, were based on those reported in NPL Good Practice Guide 119 [3] and the method reported in Reference [4].

Table 3. Uncertainty sources and calculation method used to determine the combined standard uncertainty of nanoparticle diameter measurements.

Input quantity x_i	**Distrib / Type**	**Method**	**Uncertainty contribution $u(x_i)$ / unit**	**Sensitivity coefficient c_i / unit**	**Reference**
Pixel pitch in the x-direction	N/B	Calibrated using Pelcotec line artefact	/ nm per pixel	= particle diameter / pixels	
Pixel pitch in the y-direction	N/B	Calibrated using Pelcotec line artefact	/ nm per pixel	= particle diameter / pixels	
Background signal level	N/B	Standard deviation of pixel grey levels in background, measured from one representative image per sample	/ grey levels	1/ (intensity gradient at particle boundary / grey levels per nm)	
Signal level at particle centre	N/B	Standard deviation of pixel grey levels inside particle, measured from one representative particle per sample	/ grey levels	1/(intensity gradient at particle boundary / grey levels per nm)	
Local threshold level	R/B	Full range = mean diameter measured from local threshold levels of 0.45 and 0.55 Plateau in transmitted signal fraction at particle boundary is between 0.45 and 0.55 for Au nanoparticles at 30 kV	ui(x) = half range/√3) for a rectangular distribution / nm	1	Meli et al. 2012 [4]
Image digitisation	N/B	ɔr a circle of diameter, d_c, andard deviation of n_c ma $\sigma(n_c) = 0{,}68\left(\frac{d_c}{2}\right)^{\frac{1}{2}}$ ıe number of pixels, n_c, to l r any standard deviation	/ pixels	1	ISO 13322-1: 2014(E) [5]
Combined standard uncertainty $u_c(d)$ = Add in quadrature					

5.4. RESULTS

5.4.1. Au60

Figure 6a-c) show an example of the 308 images acquired for the Au60 sample with just a couple of particles visible. Figure 6d) shows an image of a representative particle and its detected edge position. White pixels have an intensity value of 1, and black pixels have an intensity value of 0. The blue to yellow colour scale shows the fractional threshold values of the contour lines. Edge positions at fractional threshold values of 0.45, 0.50 and 0.55 are shown by the blue, green and yellow contour lines respectively. The contour lines are close together, which shows that the measured particle size is relatively insensitive to the choice of threshold value between 0.45 and 0.55.

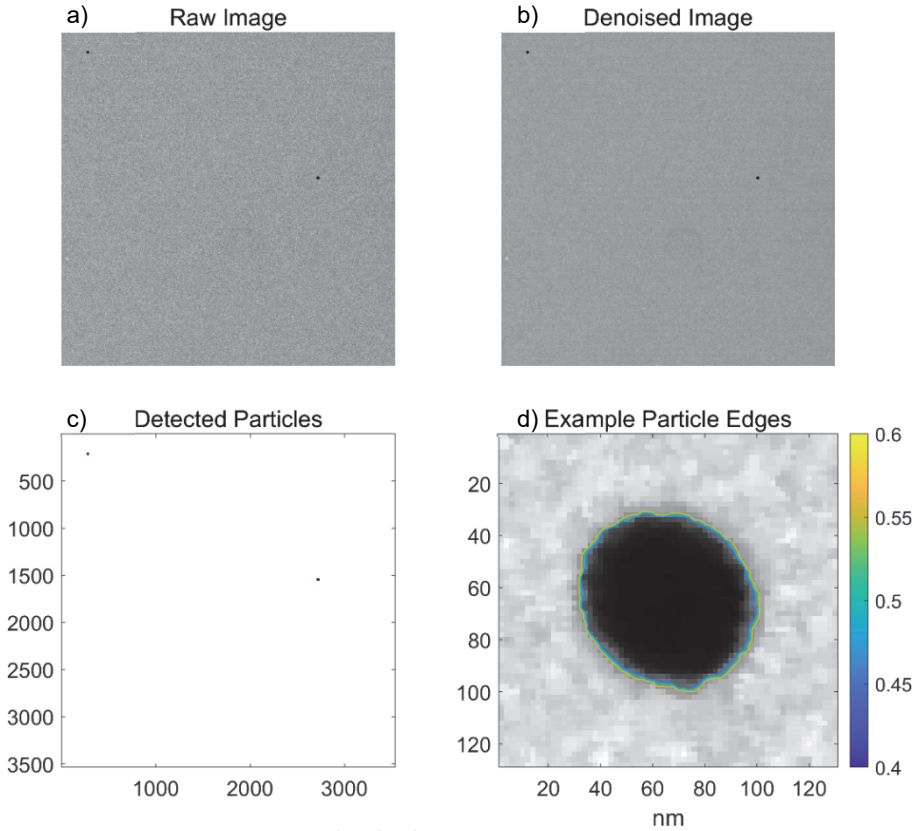

Figure 6. Representative BF-TSEM image (a-c) of the 308 images acquired and example particle boundary (d) of a single Au60 nanoparticle.

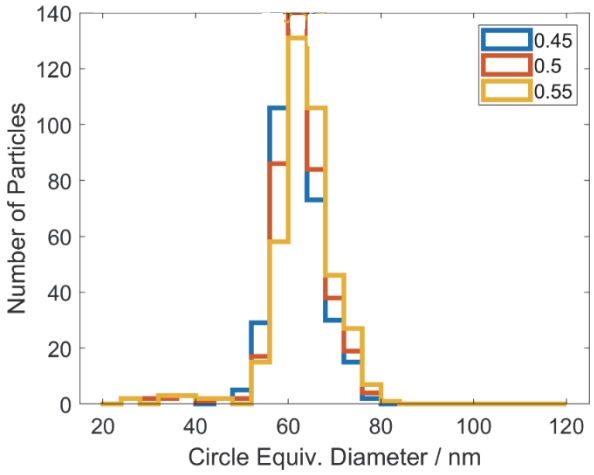

Figure 7. Measured particle size distributions of Au60 gold nanoparticles for the three different fractional thresholds used.

Figure 7 shows the resulting particle size distributions measured using the three different fractional thresholds of 0.45,0.5 and 0.55. The mean values are 61.2,62.3 and 63.5 nm for the 0.45,0.50,0.55 thresholds respectively, so applying the formula in Table 3 for local threshold levels, the standard uncertainty contribution from this is ½ (63.5-61.2)/ √3 = 0.66 nm.

Table 4 shows this value and the other contributions to the total uncertainty outlined in Table 3. From this the combined standard uncertainty for the mean particle diameter is 1.30 nm (k = 1). Because of the contributions of the signal level and threshold to the uncertainty, even if there were no uncertainty in the x and y pixel dimensions the combined standard uncertainty would still be 1.11 nm. The standard deviation of the particle size distribution width is 6.84 nm.

Table 4. Uncertainty contributions and combined standard uncertainty of Au60 gold nanoparticles.

Input quantity x_i	Distrib/ Type	Uncertainty contribution $u(x_i)$ / unit	Sensitivity coefficient c_i / unit	Std uncertainty $u(d) = u(x_i)c_i$
Pixel pitch in the x-direction	N/B	0.64 % = 0.0128 nm per pixel	30 pixels	0.384 nm
Pixel pitch in the y-direction	N/B	0.94 % = 0.0192 nm per pixel	30 pixels	0.576 nm
Background signal level	N/B	4000 grey levels	1/ (6000 grey levels per nm)	0.67 nm
Signal level at particle centre	N/B	3500 grey levels	1/ (6000 grey levels per nm)	0.58 nm
Local threshold level	R/B	0.66 nm = $\frac{2.3\ nm}{2\sqrt{3}}$	1	0.66 nm
Image digitisation	N/B	$= 0.68 \times \sqrt{\frac{30}{2}}$ 2.63 pixels area = 0.024 pixel lengths for a 30 pixel diameter particle	1	0.048 nm
Combined standard uncertainty $u_c(d)$				1.30 nm

5.4.2. Au30

Figure 8a-c) show an example of the 96 images acquired for the Au30 sample with the much greater particle density for this sample obvious. Figure 8d) shows a representative particle plotted similarly to the particle in Figure 6d). The measured particle diameter was also close to the mean value and relatively insensitive to the choice of fractional threshold value between 0.45 and 0.55.

Figure 9 shows the resulting particle size distributions with the mean values of 31.1, 32.0 and 32.9 nm corresponding to the three different fractional thresholds of 0.45, 0.5 and 0.55 respectively. The number-weighted mean particle diameter for the 0.5 threshold is thus 32.0 nm and the

combined standard uncertainty is 1.23 nm (k = 1) as detailed in Table 5. The standard deviation of the particle size distribution width is 2.82 nm which is in good agreement with the particle size of 32.7 ± 2.0 nm (k=2), measured independently by particle tracking analysis.

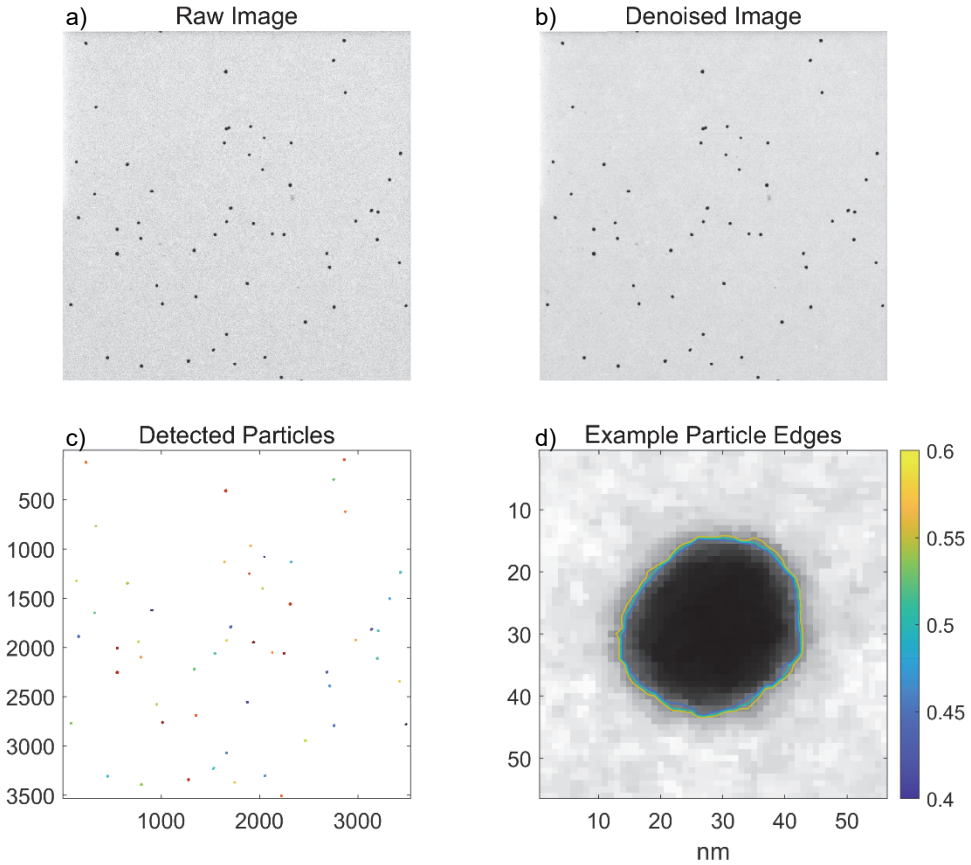

Figure 8. Representative BF-TSEM image (a-c) of the 96 images and an example particle boundary (d) of a single Au30 nanoparticle.

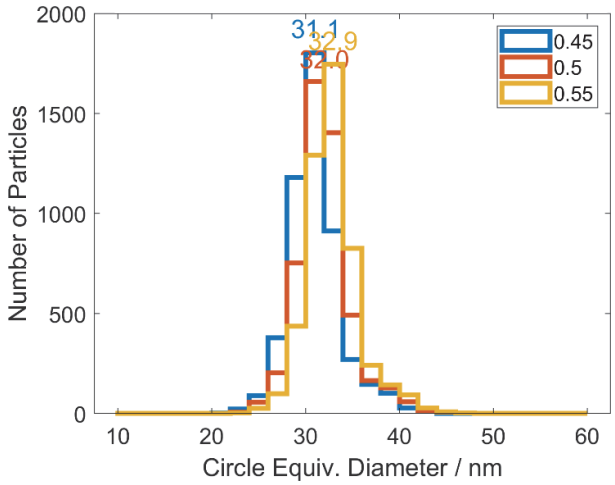

Figure 9. Measured particle size distributions of Au30 gold nanoparticles for the three different fractional thresholds used.

Table 5. Uncertainty contributions and combined standard uncertainty of Au30 gold nanoparticles.

Input quantity	Distrib/ Type	Uncertainty contribution $u(x_i)$ / unit	Sensitivity coefficient c_i / unit	Std uncertainty u(d) / nm
Pixel pitch in the x-direction	N/B	0.0075 nm per pixel length	30 pixel lengths	0.225 nm
Pixel pitch in the y-direction	N/B	0.0094 nm per pixel length	30 pixel lengths	0.282 nm
Background signal level	N/B	2000 grey levels	3400 grey levels per nm	0.58 nm
Signal level at particle centre	N/B	3000 grey levels	3400 grey levels per nm	0.88 nm
Local threshold level	R/B	0.52 nm = $\frac{1.8\ nm}{2\sqrt{3}}$	1	0.52 nm
Image digitisation	N/B	$2.63 = 0.68 \times \sqrt{\frac{30}{2}}$ 2.63 pixels area = 0.024 pixel lengths for a 30 pixel diameter particle	1	0.024 nm
Combined standard uncertainty $u_c(d)$				1.23

6. ANGULAR MEASUREMENT BY EBSD

6.1. EBSD ORIENTATION UNCERTAINTY CONTRIBUTIONS

Measurement uncertainty in EBSD has both bias and precision components. Bias affects absolute orientation measurements but not misorientations measured within a single EBSD map, whereas precision affects both absolute orientation and misorientation metrics such as kernel average misorientations (KAM), grain reference orientation deviations (GROD), and grain boundary misorientations.

Uncertainties related to measurement bias are dominated by small misalignments between the physical sample axes, the prepared sample surface, and the nominal sample geometry assumed by the orientation indexing software. This is conventionally accepted to be around ± 2° but not systematically reported in published literature [6]. Uncertainties related to precision are caused by beam shifts in wide area EBSD mapping and uncertainties in detecting and fitting Kikuchi bands. The magnitude depends on the EBSD pattern postprocessing and orientation indexing method, are around ≤ ± 0.5° for most conventional EBSD pattern indexing methods [7-13].

Orientation reporting errors that are unrelated to the EBSD measurement uncertainty can also arise when using third party software to analyse or visualise EBSD data, such as through inverse pole figure (IPF) direction orientation maps or pole figures. This is because the system-specific SEM-EBSD coordinates axis conventions are required to plot EBSD data correctly, and these conventions must be explicitly defined when importing EBSD data into third-party software.

6.2. METHOD

6.2.1. Experimental setup

Similar EBSD maps from three different SEM and EBSD systems were acquired from the same sample. Figure 10 shows EBSD pattern quality maps acquired from (A) a Zeiss Supra 40 SEM / EDAX Hikari EBSD detector, (B) a ThermoFisher Apreo 2S SEM / EDAX Velocity Plus EBSD detector, and (C) a Zeiss Auriga 60 SEM / Oxford Instruments Symmetry2 EBSD detector respectively.

The orientation data files were exported from all three SEM systems and imported into MTEX.
An MTEX implementation of the TrueEBSD method [14] was used to spatially align the EBSD maps to the reference backscatter electron image Figure 10(E) acquired at 0° sample tilt using the Apreo T1 detector, using (D) a forescatter electron image acquired at 70° sample tilt using the Symmetry2 EBSD detector, in the EBSD map acquisition geometry, as an intermediate image.

The sample is the corner of a platinum foil glued on to a standard aluminium pin stub using silver paint. The stub diameter is 12.5 mm, pin diameter is 3.2 mm, and pin length is 8 mm. Figure 10(F) shows the EBSD map region of interest in a low-magnification SEM image. The pin stub is fixed to the SEM sample holder by a M1.6 grub screw on the side of a pin hole. For the two Zeiss SEMs, the SEM sample holder is fixed to the SEM stage by a dovetail plate. For the Apreo SEM two pin stubs were used in series: the first attached to the sample and the other as a height spacer to avoid the EBSD detector crashing into the SEM stage. The SEM sample holder is fixed to the SEM stage by a central M5 screw. The sample stages and holders are wide and shallow compared to the pin stub, and the mechanical contact is more constrained (2 points + 2 faces for the Zeiss dovetail joint and 1 M5 screw thread + 1 face for the Apreo stage, versus 1 line + 1 point for the pin stub), therefore any mechanical misalignment from sample loading is probably dominated by misalignment of the pin stub(s).

All EBSD maps were acquired with 20 kV electrons and high probe currents. Pt has a high backscattering coefficient due to its high atomic number and density, which means the effect of carbon contamination buildup due to repeated EBSD mapping on EBSD pattern quality is negligible.

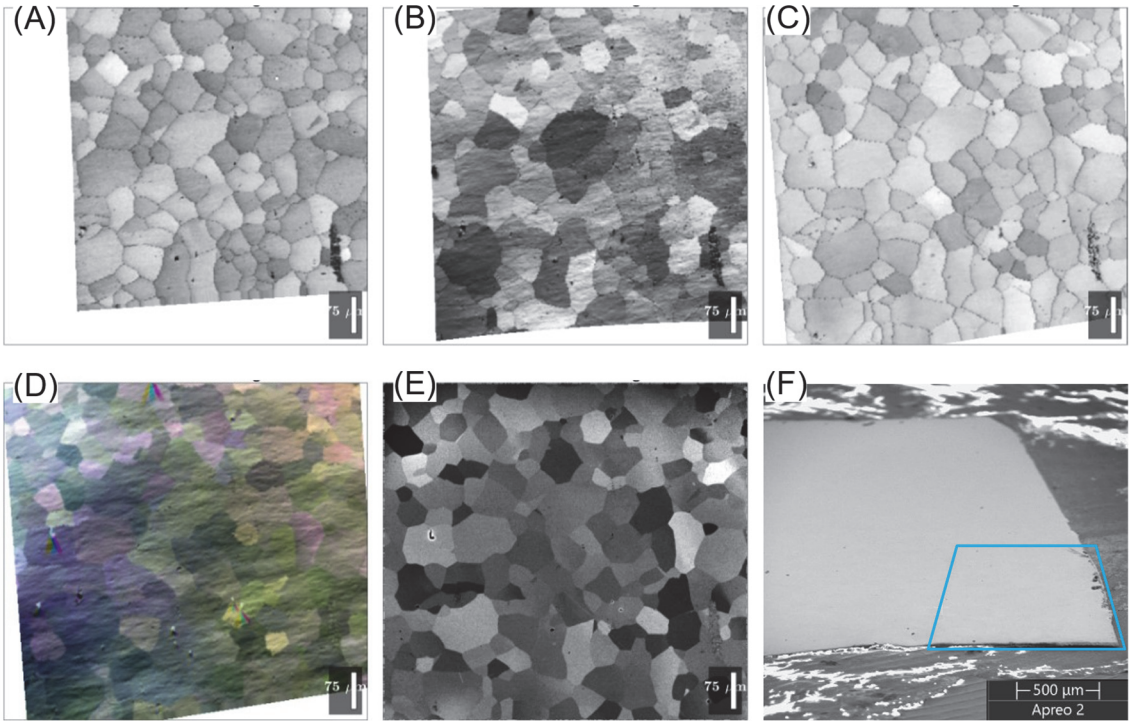

Figure 10. Images used for (A-C) EBSD pattern quality maps maps acquired from three different SEM-EBSD systems; (D) Forescatter electron image acquired in the same SEM-EBSD geometry as the EBSD map in (C); (E) Backscatter electron image acquired from a ThermoFisher Apreo SEM at 0° sample tilt using the T1 detector; (F) A low-magnification SEM image showing the Pt foil sample attached to an aluminium pin stub using silver paint. The sample region of interest for all three EBSD maps is outlined in blue. The trapezoidal distortion is due to the high sample tilt angle (70°) and large image field of view.

6.3. RESULTS

6.3.1. Pt polycrystal orientation maps

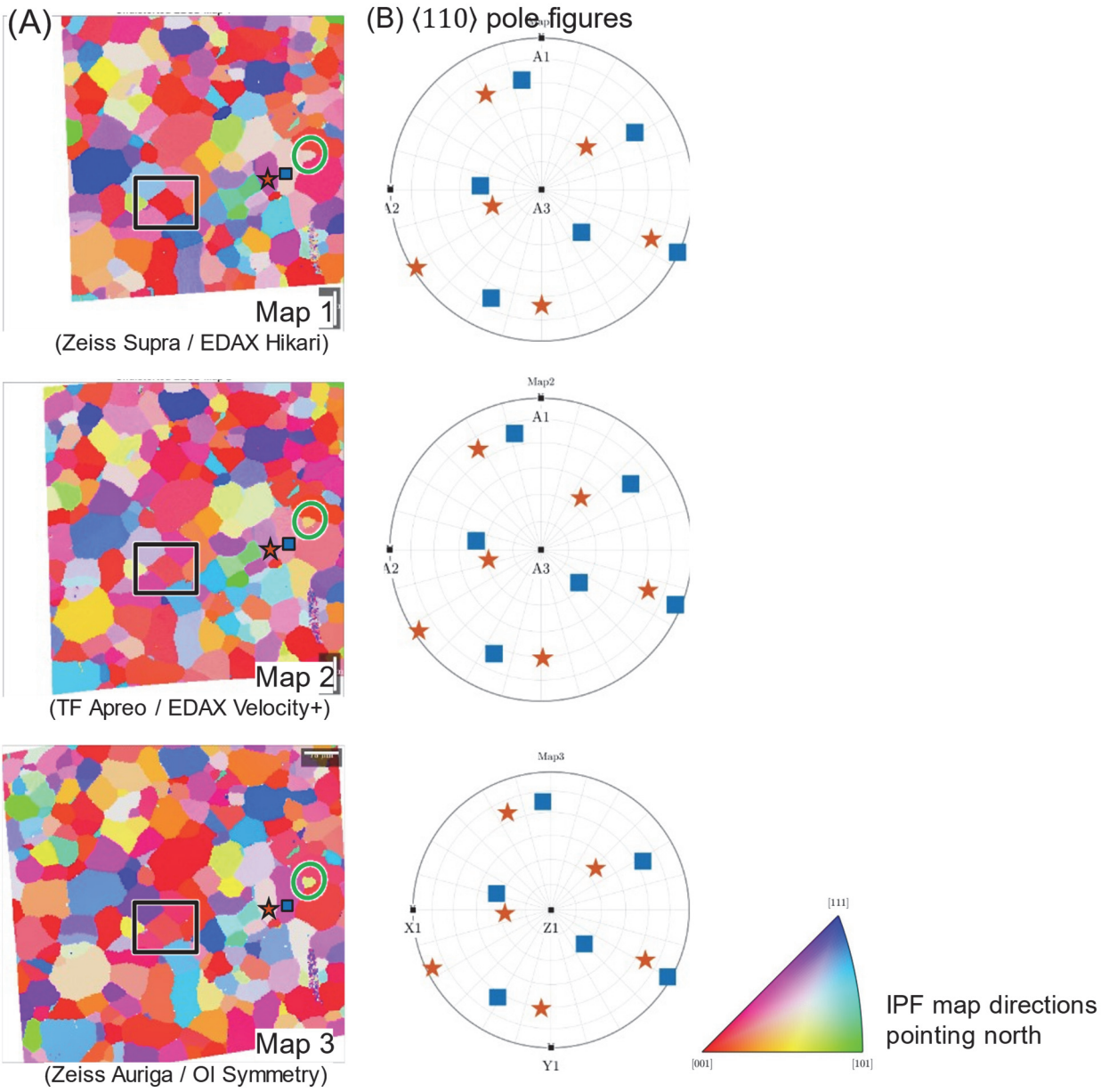

Figure 11.– (A) EBSD orientation maps showing IPF directions point north (up) in the page; (B) Pole figures showing <110> crystal directions of two points annotated with a red star and blue square in (A). The spherical grid is in equal area projection and the line pitch is 15°. EBSD sample coordinate axes are labelled according to the EBSD manufacturer conventions (A1/A2/A3 for EDAX systems, X1/Y1/Z1 for Oxford Instrument systems).

Figure 11(A) shows EBSD orientation maps from the three SEM and EBSD systems, where inverse pole figure (IPF) colours [15] show the Pt crystal directions pointing out-of-screen. The IPF colours and grain structures in all EBSD maps are similar because they are from the same sample area.

Small orientation changes (such as the presence of low-angle grain boundaries) should not be analysed using IPF maps, because the colour variations are not perceptually uniform. The three EBSD maps are related to each other by rigid body rotations of 5-8°, as will be shown later in Figure 12, but colour changes near the centre of the IPF triangle are more obvious than those near the corners. For

example, in the area marked by the black rectangle, the colour contrast across grain boundaries is much stronger for Map 1 than Map 3. The small grain inside the green circle is bordered by three grains, but different subsets of these grain boundaries are visible as colour changes in the three EBSD maps. The colour transitions can also become perceptually misleading when the IPF directions are near the edge of a fundamental zone, such as for the pair of grains marked with the brown star and blue square. Figure 11(B) shows pole figures of the <110> crystal directions corresponding to these two orientations; they are slightly rotated between EBSD maps but the misorientation between them is the same. However, the IPF colours in Figure 11(A) are very different, and even appear switched between Map 1 and Map 3 (pink and light brown in Map 1, versus light brown and pink in Map 3).

The pole figures in Figure 11(B) show <110> crystal directions in the EBSD image coordinate frame. The pole figures are plotted with the same image orientation as the EBSD maps, and the EBSD sample coordinate axes (A1/A2/A3 or X1/Y1/Z1) are labelled on the image. The sample coordinate axes differ between EBSD manufacturers, and are required for correct interpretation of the Euler angles (which describe rotations about Z-X-Z' sample axes when using the Bunge convention).

6.3.2. Absolute orientation uncertainty

Point-to-point misorientations between the three maps were used to determine the orientation uncertainty contribution due to SEM and sample misalignments.

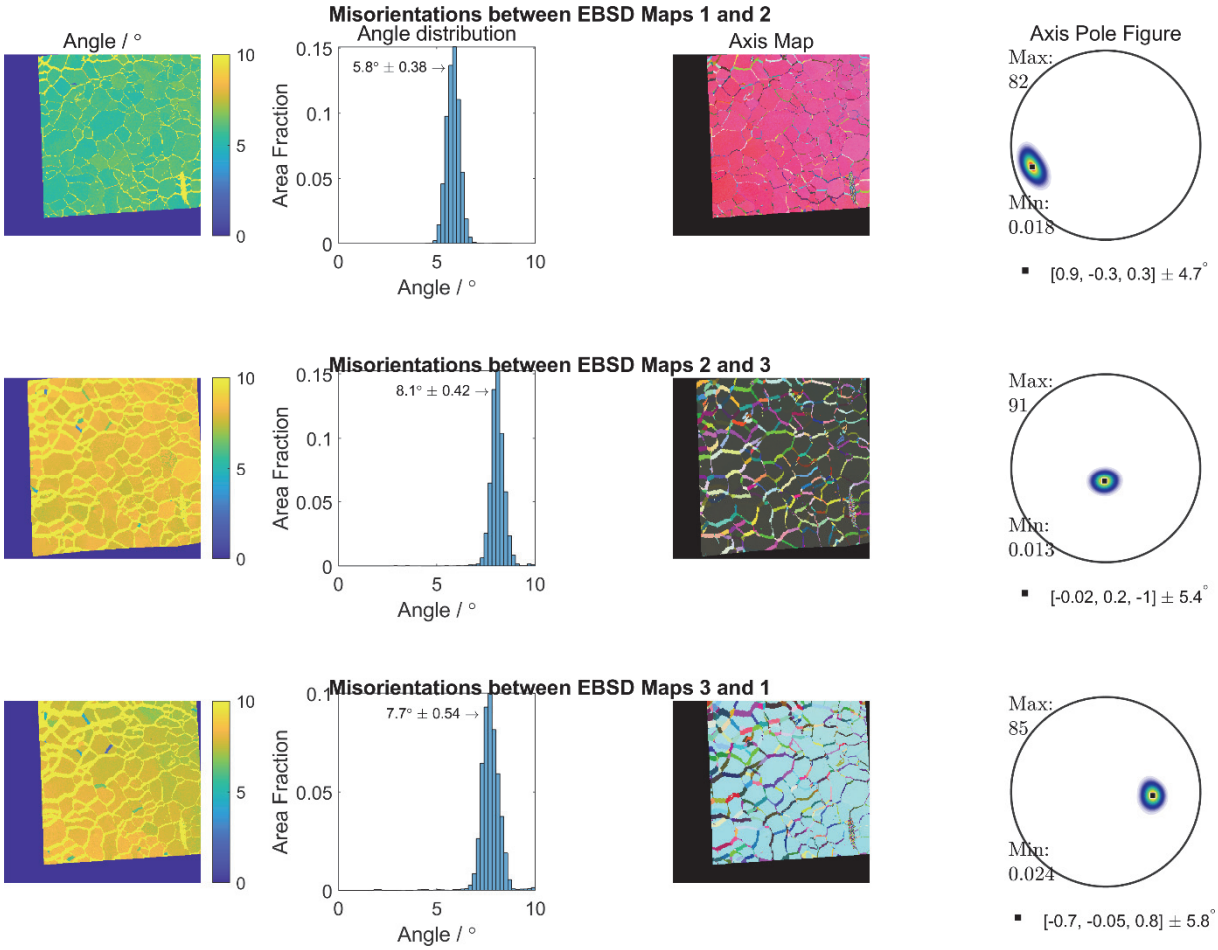

Figure 12. Point-to-point comparisons of EBSD orientations acquired from three different SEM and EBSD systems. Histogram annotations are the mean and standard deviation of the misorientation angle between EBSD map pairs, with intergranular regions (> 10°) filtered out.

Figure 12 shows the point-to-point misorientation angles and axes of three EBSD maps presented in Figure 10. Regions of high misorientation angle > 10° at grain boundaries are due to errors in image registration between EBSD maps. (These errors could have been reduced by acquiring intermediate images at 0° and 70° from each of the image registration steps, but are adequate for the present study.)

The absolute orientation uncertainty is ± 8° for routine EBSD mapping without applying any scan direction alignment or special calibration procedures such as the one suggested in Reference [16]. The orientation deviation between maps is uniform across the map field of view, which means that they are mainly due to rigid body rotations of the sample between the different SEMs. Figure 13(A) shows the possible origins of sample misalignment in the SEM. These misalignments are small in well-prepared samples, most likely less than 5°, but the affine image distortions arising from these small misalignments are amplified by the 70° stage tilt required for EBSD mapping.

Reference [16] shows that a 2° rotation of the sample surface around the tilt-foreshortened direction leads to a 7° apparent rotation of the tilt axis in the SEM image. This means that a 2° sample misalignment can cause a 7° error when the SEM operator tries to rotate the stage to align the SEM image to the stage axes. Additional image distortions arising at high tilt angles, such as the scan rotation distortions caused by dynamic focussing (Figure 2), also contribute to this uncertainty. This is consistent with Figure 12, which measure rigid body rotations of 5 - 8° between different EBSD maps.

Figure 13(B) and (C) shows the nominal sample surface and EBSD camera geometry expected by the EBSD software. These parameters are typically determined during installation of the EBSD system using a single-crystal silicon wafer as a calibration sample, which has parallel sides and well-known cleavage planes with known absolute orientation. However, the sample is still glued onto a pin stub and screwed into a SEM holder, and therefore susceptible to absolute orientation uncertainty, which propagates to all orientation measurements.

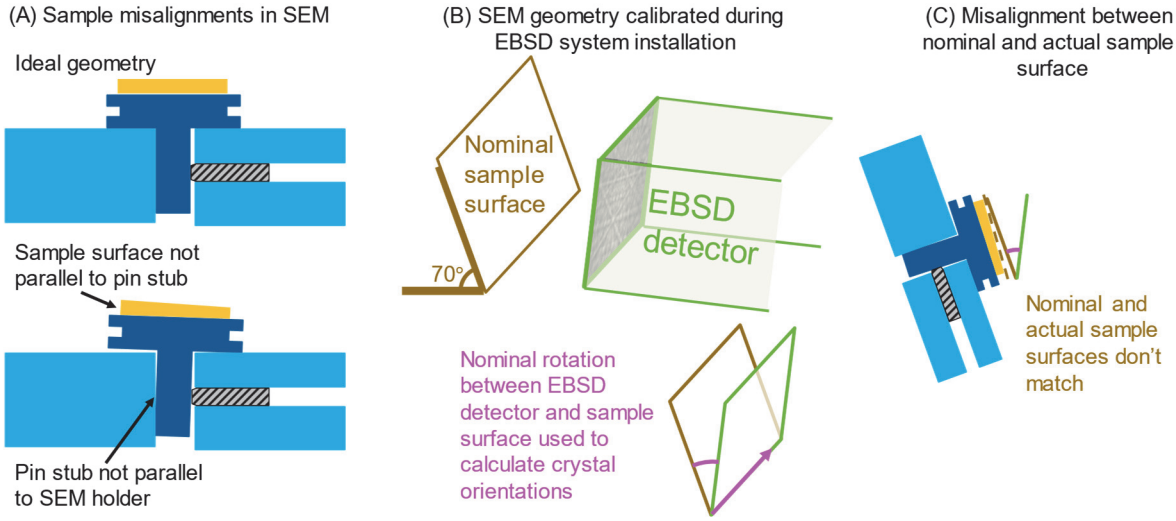

Figure 13. (A) Origin of sample misalignments in SEM; (B) The SEM geometry assumed by the EBSD software. The rotation between the EBSD detector and nominal sample surface; (C) Misalignments between

6.3.3. EBSD coordinate calibrations

Accurate description of a crystal orientation measured using EBSD requires (1) the sample orientation (e.g. relative to sheet rolling or wire drawing directions) to be related to the (2)

crystallographic orientations, via the (3) SEM stage axes, (4) SEM image scan directions, and (5) EBSD camera orientation. The relationship between these five coordinate systems needs to be calibrated independently for each system. All SEM-EBSD systems reported in this work were calibrated using the method described in Reference [17] and in the EBSD user manuals supplied by Oxford Instruments and EDAX respectively. Further details are described in Appendix 2 – EBSD Coordinate calibration.

This calibration should have been performed during EBSD system installation, which means that SEM operator intervention is not necessary if only the manufacturer software is used for EBSD data analysis. However, they must be explicitly known if the orientation data is to be exported into third-party postprocessing tools for further analysis.

Coordinate system calibration was performed on all three SEM systems using the 'HKL steel' standard sample and a standard Si wafer to determine the relationships between SEM stage axes, beam scan directions, EBSD camera axes and crystal orientations. We compared the standard outputs plotted using the EBSD manufacturers' supplied software to equivalent plots produced in MTEX.

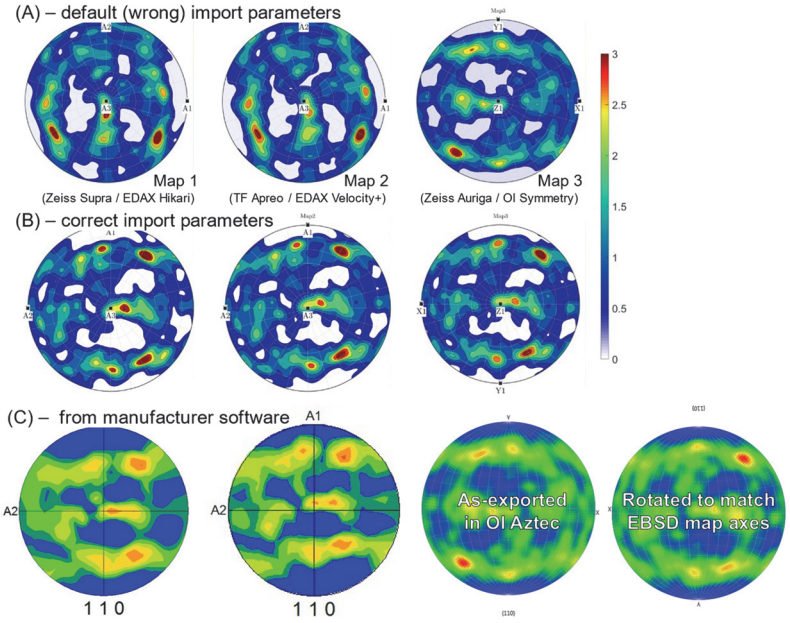

Figure 14. <110> pole figures of the EBSD maps from the same sample acquired using three different systems, (A) plotted using MTEX using the default import parameters, (B) plotted using MTEX with correct, system-specific import parameters, (C) exported from manufacturer software.

The effect of coordinate axis miscalibration on EBSD orientations is shown in Figure 14. Pole figures directly exported from all three EBSD systems are consistent with each other, but pole figures plotted in MTEX are consistent only if the data was imported with the correct reference coordinate geometries determined by the calibration procedure.

Figure 14 shows <110> pole figures plotted in MTEX using (A) incorrect and (B) correct import parameters, with (C) equivalent pole figures generated by manufacturer-supplied software. The pole figures in subfigure (A) do not match each other, nor do they match the manufacturer-exported pole figures in (C). In contrast, the pole figures in (B) match each other and the pole figures in (C). Note that the Oxford Instruments Aztec software plots pole figures 'upside-down' relative to their EBSD maps: in Aztec pole figures, X points East and Y points north; in Aztec EBSD maps, X points West and

Y points South. This is consistent with the Aztec annotation labels. A 180° rotation of the pole figure image is required to match the EBSD map X1 and Y1 axes.

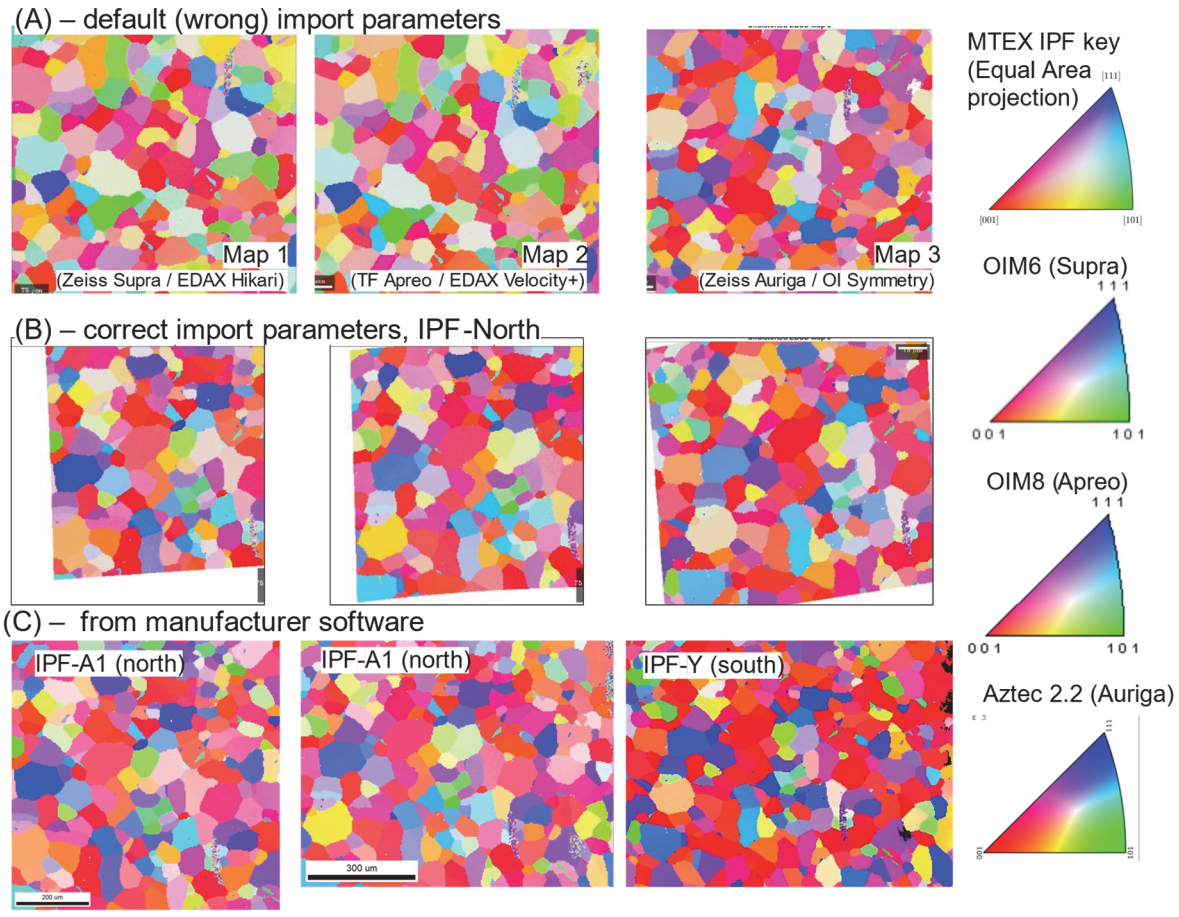

Figure 15. IPF-North EBSD orientation maps of the same sample acquired using three different systems, (A) plotted using MTEX using the default import parameters, (B) plotted using MTEX with correct, system-specific import parameters, (C) exported from manufacturer software. Note that IPF colour key used by the manufacturers (bottom) is has slightly different colour transitions to the one used in MTEX (top).

Figure 15 shows a similar effect of using the wrong import parameters for EBSD orientation map plots. The correct import parameters are required for correct plotting of IPF maps in MTEX, and this can be checked by comparing with the manufacturer software-exported maps. The IPF colour keys differ between analysis softwares (even different versions of OIM [18]), so small differences in IPF colour for a given orientation can be expected.

6.4. PRACTICAL CONSIDERATIONS FOR EBSD ALIGNMENT AND PLOTTING

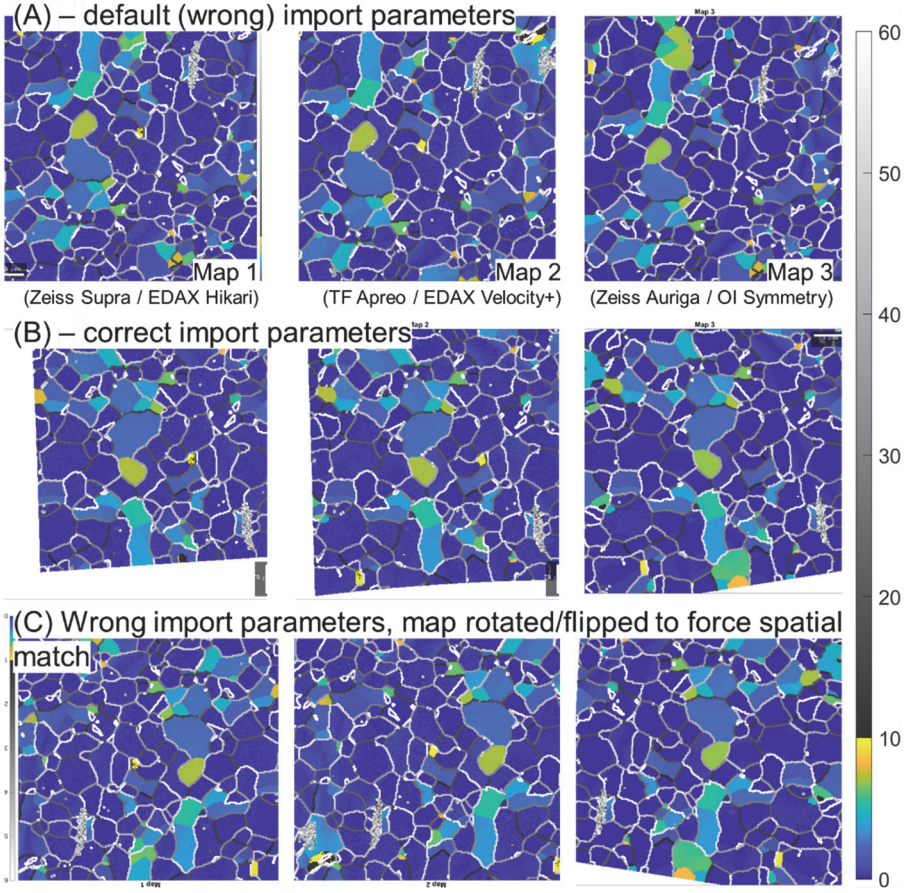

Figure 16. Grain reference orientation deviation (GROD) angle and grain boundary misorientation angle maps. The colour scale is in degrees. (A) When the wrong import parameters are used, the maps appear rotated or flipped, but the misorientation angle values are correct (B), and (C) can be forced to match the correctly imported data simply by rotation or flipping the map plots.

EBSD is used for a wide range of microstructural analysis applications, and accurate knowledge of the absolute crystal orientations is only sometimes required. Correct calibration of the SEM-EBSD coordinates is required only in applications where the absolute orientations need to be correct.

Figure 16 shows that for grain size analysis or KAM / GROD angle analysis, only the misorientations angles are required, and therefore the absolute orientations do not matter. Applications which require the misorientation axis in crystal coordinates only, such as twin or special boundary identification, are also insensitive to absolute orientation errors. However, correct absolute orientations are required if the misorientation axes are related back to spatial features on the sample, such as for grain boundary trace or slip trace analysis.

Absolute orientations need to be correct for texture analysis in general. However, errors in absolute orientation due to errors in relationship between EBSD coordinate systems can be often hidden in crystallographic texture analysis, because textures arising from sample processing often inherit the symmetry of the processing method: for example, drawn wires have a fibre crystallographic texture with radial symmetry around the wire axis. The orientation distribution functions or pole figure plots will therefore appear plausible due to the overlap between symmetry operators in the sample and the SEM and EBSD axes. Small biases in the measured orientations due to the sample misalignments described in Figure 13 will be visible as small rotations of the orientation distribution function, as long as it is not hidden by a symmetry operator of the orientation distribution function.

7. SUMMARY

7.1. DIMENSIONAL MEASUREMENTS

- Errors in the dimensional calibration of a range of modern scanning electron microscopes have been shown to be less than 2% and in many cases less than 1% for samples oriented normally to the beam.
- In general errors are greatest at lower magnifications, for a wide range of conditions from low kV and short working distances to high kV and long working distances.
- Calibration errors change significantly when the calibration sample is tilted to high angles (>30°). However the results obtained suggest these errors may be strongly affected by small (unquantified) changes in the way the sample is mounted and fixed in the microscope which alter the true tilt angle.
- Even when measuring digital images using a fixed pixel size, there can be operator bias which can double the measurement error. This is particularly significant at very high magnifications/small pixel sizes when only a few calibration sample lines are visible and/or there is a tendency for sample drift perpendicular to the linear calibration features.
- Dimensional calibration errors are only one factor in the uncertainty of a dimensional measurement from an image. The examples shown in Section 4 demonstrate that the variation in sample and background signal and choice of threshold all have similar or greater contributions to the uncertainty.

7.2. ANGULAR MEASUREMENTS

- The absolute orientation uncertainty has been shown to be typically ± 8° for routine EBSD mapping without applying any scan direction alignment or special calibration procedures, and is dominated by uncertainty in SEM sample alignment.
- This can lead to apparent large and variable perceived differences in IPF colour maps, especially when coupled with different IPF colour scales and at locations close to edges of the fundamental zone.
- Precise knowledge of the absolute orientation is not required for grain size measurements or misorientation angle analyses.

Acknowledgements
Extensive measurements by Abdalrhaman M. Koko and Mark Stewart and additional help by Helen Jones and Hannah Zhang all contributed to the results presented in this report. Additional data analysis by Mark Stewart and critical analysis by Mark Gee are gratefully acknowledged.

8. REFERENCES

1. ISO 16700:2016 Microbeam analysis Scanning electron microscopy Guidelines for calibrating image magnification, https://www.iso.org/standard/65375.html
2. ASTM E766-14 Standard Practice for Calibrating the Magnification of a Scanning Electron Microscope, ASTM International, 100 Barr Harbor Drive, PO Box C700, West Conshohocken, PA 19428-2959. United States
3. Good Practice Guide for the Determination of the Size and Size Distribution of Spherical Nanoparticle samples, R.D. Boyd, A. Cuenat, F. Meli, T. Klein, C.G. Frase, G. Gleber, M.Krumrey, A. Duta, S. Duta, R. Hogstrom and E. Prieto, GPG119, https://eprintspublications.npl.co.uk/5444/1/mgpg119.pdf
4. Traceable size determination of nanoparticles, a comparison among European metrology institutes, F. Meli, T. Klein, E. Buhr, C.G. Frase, G. Gleber, M. Krumrey, A. Duta, S. Duta, V. Korpelainen, R. Bellotti, G.B. Picotto, R.D. Boyd, A. Cuenat, , Meas. Sci. Technol. 23 (2012). https://doi.org/10.1088/0957-0233/23/12/125005.
5. ISO 13322-1:2014 Particle size analysis — Image analysis methods Part 1: Static image analysis methods, 2014. https://www.iso.org/standard/51257.html
6. HUMPHREYS, F. J. (1999). Quantitative metallography by electron backscattered diffraction. Journal of Microscopy, 195(3), 170–185. https://doi.org/10.1046/j.1365-2818.1999.00578.x
7. Humphreys, F. J. (2001). Grain and subgrain characterisation by electron backscatter diffraction. Journal of Materials Science, 36(16), 3833–3854. https://doi.org/10.1023/A:1017973432592
8. Brough, I., Bate, P. S., & Humphreys, F. J. (2006). Optimising the angular resolution of EBSD. Materials Science and Technology, 22(11), 1279–1286. https://doi.org/10.1179/174328406X130902
9. Winkelmann, A., Jablon, B. M., Tong, V. S., Trager-Cowan, C., & Mingard, K. P. (2020). Improving EBSD precision by orientation refinement with full pattern matching. Journal of Microscopy, 277(2), 79–92. https://doi.org/10.1111/jmi.12870
10. Maurice, C., & Fortunier, R. (2008). A 3D Hough transform for indexing EBSD and Kossel patterns. Journal of Microscopy, 230(3), 520–529. https://doi.org/10.1111/j.1365-2818.2008.02045.x
11. Nolze, G., & Winkelmann, A. (2020). About the reliability of EBSD measurements: Data enhancement. IOP Conference Series: Materials Science and Engineering, 891(1), 012018. https://doi.org/10.1088/1757-899X/891/1/012018
12. Wright, S. I., Nowell, M. M., Lindeman, S. P., Camus, P. P., De Graef, M., & Jackson, M. A. (2015). Introduction and comparison of new EBSD post-processing methodologies. Ultramicroscopy, 159, 81–94. https://doi.org/10.1016/j.ultramic.2015.08.001
13. Thomsen, K., Schmidt, N. H., Bewick, A., Larsen, K., & Goulden, J. (2013). Improving the Accuracy of Orientation Measurements using EBSD. Microscopy and Microanalysis, 19(S2), 724–725. https://doi.org/10.1017/s1431927613005618
14. Tong, V. S., & Ben Britton, T. (2021). TrueEBSD: Correcting spatial distortions in electron backscatter diffraction maps. Ultramicroscopy, 221. https://doi.org/10.1016/j.ultramic.2020.113130
15. Nolze, G., & Hielscher, R. (2016). Orientations – perfectly colored. Journal of Applied Crystallography, 49(5), 1786–1802. https://doi.org/10.1107/s1600576716012942
16. Nolze, G. (2007). Image distortions in SEM and their influences on EBSD measurements. Ultramicroscopy, 107(2–3), 172–183. https://doi.org/10.1016/j.ultramic.2006.07.003

17. Britton, T. B., Jiang, J., Guo, Y., Vilalta-Clemente, A., Wallis, D., Hansen, L. N., Winkelmann, A., & Wilkinson, A. J. (2016). Tutorial: Crystal orientations and EBSD - Or which way is up? Materials Characterization, 117, 113–126. https://doi.org/10.1016/j.matchar.2016.04.008
18. https://edaxblog.com/2022/10/04/improved-ipf-color-palettes/ [accessed 2024-02-26]

9. APPENDIX 1 – SEM CAPABILITIES

Four scanning electron microscopes (SEM) are routinely used for microstructural characterisation at NPL. We want to ensure that any conclusions about a material's microstructure are independent of the measurement device.
The comparison described previously used the following SEMs. The SEMs and auxilliary equipment are from different manufacturers and use significantly different backend technologies to produce the final image, as well as different names and abbreviations to describe closely related or identical features.

Table 1 SEMs used for microstructural characterisation at NPL.

	Zeiss Supra 40	Zeiss Auriga 60	Zeiss Evo	ThermoFisher Apreo 2s
Electron beam generation	Field emission gun Gemini I column [8kV beam booster for <20 kV with electrostatic lens at objective lens exit, beam deflection through multihole aperture]	Field emission gun Gemini I column [as Supra] (Focussed ion beam also available, not covered in this report)	W-cathode with ion getter pump Manual positioning of 20 and 30 µm apertures Environmental SEM up to 2000 Pa, but low vac not a subject in this study	Field emission gun Magnetic/electro static final lens with additional immersion lens Low-vacuum SEM up to 500 Pa with aperture, but low vac not a subject in this study
Microscope stage	+/- 65 mm in X and Y 0-50 mm in Z -4° to +70°Tilt, full 360° rotation range]	+/- 75 mm in X and Y 0-50 mm in Z and 0-13 mm in M for eucentric height setting -15° to +70°Tilt, full 360° rotation range]	+/- 50 mm in X +/- 62.5 mm in Y 0-25 mm in Z 0° to +90°Tilt, full 360° rotation range]	+/- 55 mm in X and Y 0-66 mm in Z -15° to +90°Tilt, full 360° rotation range]
Imaging detectors	SE2 (Everhard Thornley type)	SESI (Secondary electron/ secondary ion)	SE2 (Everhard Thornley type)	ETD (Everhard Thornley) T1
Energy dispersive X-ray spectroscopy (EDS or EDX)	Oxford Instruments X-Max 50 running INCA software	Oxford Instruments X-max 80 running Aztec 6 software	Oxford Instruments X-max 80 running Aztec 3.1 software	EDAX Octane Elect Super running Apex 2.5software
Electron backscatter diffraction (EBSD)	EDAX-TSL Hikari camera running OIM 6 software Single-diode forescatter imaging detector	Oxford Instruments Symmetry 2 camera running Aztec 6 software 5-diode forescatter imaging detector	--	EDAX Velocity Plus camera running Apex 2.5 software

	Zeiss Supra 40	Zeiss Auriga 60	Zeiss Evo	ThermoFisher Apreo 2s
Compatible substages	Scratch testing High-stiffness wedge indenter for in-situ crack propagation	Nanoindentationi ncluding micro-mechanical testing of µm-scale samples (Asmec nanoindenter) Heating and liquid nitrogen cooling stage [temperature range?]	Peltier cooling stage	Deben MT2000E micro-mechanical test stage for mm-scale samples up to 300 °C and 2 kN

10. APPENDIX 2 – EBSD COORDINATE CALIBRATION

10.1. SEM STAGE, IMAGE AND EBSD COORDINATES

The 'HKL Steel' sample supplied by Oxford Instruments was used as a calibration artefact to relate the orientation of the sample in the SEM chamber to the coordinates of the SEM image.

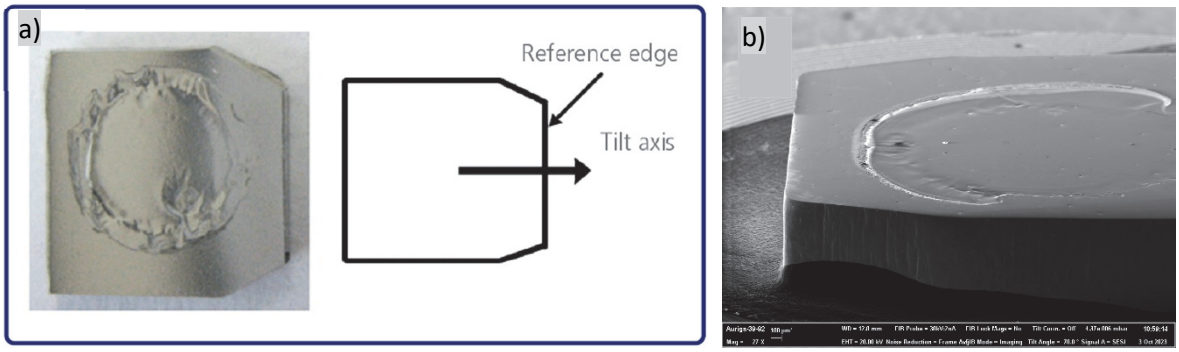

Figure 1 HKL Steel sample a) schematic supplied by Oxford Instruments in the AztecCrystal User Guide, showing sample orientation in the SEM chamber as viewed from behind the EBSD detector; b) imaged in the Auriga at 70° stage tilt.

	Zeiss Supra	Zeiss Auriga	ThermoFisher Apreo
SEM chamber axes	(same as Apreo)	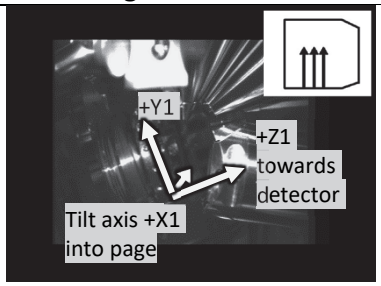	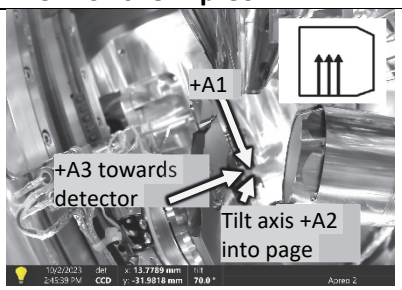
Cartesian EBSD axes	(same as Apreo)	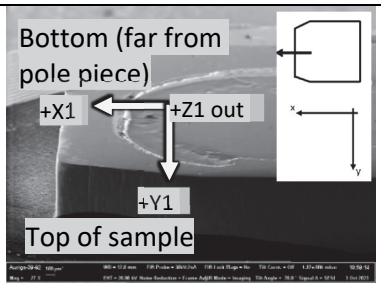	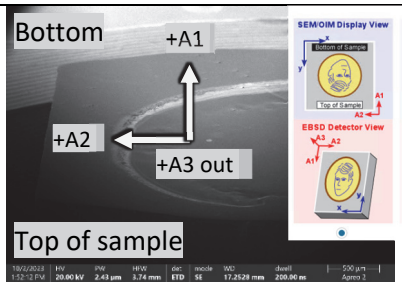
Map image coordinates (defined convention)	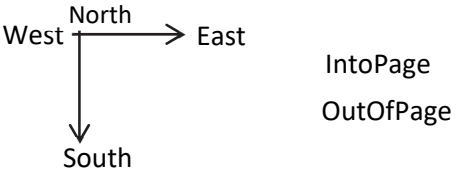		

10.2. EULER ANGLE REPORTING CONVENTIONS

Euler angles are reported as passive rotations using the Bunge convention, so $[\phi_1, \Phi, \phi_2]$ = passive rotations around the [Z1, X1, Z1] axes respectively for the Oxford Instruments system, or [A3, A1, A3] for the EDAX systems. These are not equivalent rotations, since A1 and X1 are different directions on the physical sample. This difference is hidden on the Si wafer sample, because the A1 and X1 directions are related by crystal symmetry – in this case, both are aligned to $\langle 110 \rangle$ directions 90° apart on the Si wafer.

	Zeiss Supra	**Zeiss Auriga**	**ThermoFisher Apreo**
Euler angles on Si wafer with ⟨110⟩ ‖ West; (001) ‖ OutOfPage	[225°, 95°, 357°]	[*x*°, 2°, 43-*x*°] where 0°<*x*<43°	[136°, 92°, 180°]